Chemical Science

ROYAL SOCIETY OF CHEMISTRY

EDGE ARTICLE

View Article Online
View Journal | View Issue



Cite this: *Chem. Sci.*, 2025, **16**, 21600

All publication charges for this article have been paid for by the Royal Society of Chemistry

# Linker desymmetrisation unlocks new topologies, defective clusters, and catalytic activity in zirconium- and rare-earth metal–organic frameworks

Borja Ortín-Rubio, †[abc] Yunhui Yang,†[ab] Emilio Borrego-Marin, [d] Jaume Rostoll-Berenguer,[e] Carlos Vila, [e] Judith Juanhuix, [f] Inhar Imaz,*[ab] Jorge A. R. Navarro [d] and Daniel Maspoch *[abg]

Metal–organic frameworks (MOFs) based on highly connected nets continue to expand the landscape of reticular chemistry, with zirconium (Zr) and rare-earth (RE) clusters offering ideal nodes for the construction of robust and structurally diverse materials. While desymmetrisation of tetratopic linkers has recently emerged as a promising approach to accessing new framework topologies, the underlying principles governing cluster connectivity remain poorly understood. Here, we systematically investigate the effect of linker desymmetrisation on the assembly of Zr- and RE-MOFs. A literature survey of planar tetratopic linkers revealed that geometric parameters such as height-to-width ratio and torsion angles play a key role in dictating cluster connectivity. Guided by these insights, we designed two new nanosized tetratopic ligands with enhanced conformational flexibility, enabling the synthesis of six MOFs with diverse cluster types and topologies. These include three Zr-MOFs, two featuring 8-connected (8-c) $Zr_6$ clusters with **csq** and **scu** topologies, and one with a rare 4-c Zr cluster, and three RE-MOFs, including one with an unprecedented heptanuclear RE cluster forming a 4,8L15 net. Finally, we demonstrate that frameworks with accessible metal clusters, such as the **csq**-Zr-MOF and 4,8L15-RE-MOF, show outstanding catalytic activity in the hydrolysis of P–F bonds in G-type nerve agent simulants. These results highlight linker desymmetrisation as a powerful strategy for tuning both structure and function in MOFs.

Received 18th July 2025
Accepted 4th October 2025

DOI: 10.1039/d5sc05365j

rsc.li/chemical-science



## Introduction

Reticular chemistry has been vastly expanded due to the virtually unlimited combinations of inorganic and organic molecular building blocks (MBBs), enabling the design of new materials with tailored chemical composition and structural properties.[1–3] This level of control has gained attention for a wide scope of applications, including molecular recognition for sensing, catalysis, gas storage and separation, as well as the removal and delivery of target compounds.[4,5] One of the most important features for these applications is the thermal and chemical stability. To address this requirement, researchers have developed strategies such as incorporating stronger coordination bonds and employing highly connected MBBs.[6–8] Particularly, the latter has emerged as a major focus in MOF chemistry over the past decade, as it facilitates the construction of highly connected nets; a key feature for building robust and stable frameworks. Furthermore, increasing the connectivity of nodes in a network reduces the number of possible topologies, thus directing the assembly toward specific structures.[7]

Several strategies have been employed to achieve highly connected nets, including the MBB approach, the supermolecular building block (SBB) strategy,[9] and the supermolecular building layer (SBL) approach.[10] Among these, the MBB approach is widely recognised as a powerful and straightforward method, enabling the successful synthesis of numerous highly connected MOFs. A major breakthrough in this area has been the discovery of polynuclear zirconium (Zr) and rare-earth (RE) clusters, which has significantly advanced the development of high-connectivity networks.[11,12] In

[a]*Catalan Institute of Nanoscience and Nanotechnology (ICN2), CSIC, The Barcelona Institute of Science and Technology, Campus UAB, Bellaterra, 08193, Barcelona, Spain. E-mail: inhar.imaz@icn2.cat; daniel.maspoch@icn2.cat*

[b]*Departament de Química, Facultat de Ciències, Universitat Autònoma de Barcelona, 08193 Bellaterra, Spain*

[c]*Max Planck Institute for Solid State Research, Heisenberstraße 1, 70569 Stuttgart, Germany*

[d]*Departamento de Química Inorgánica, Universidad de Granada, Av. Fuentenueva S/N, 18071, Granada, Spain*

[e]*Departament de Química Orgànica, Facultat de Química, Universitat de València, 46100 Burjassot, València, Spain*

[f]*ALBA Synchrotron Light Facility, Carrer de la Llum, 2-26, 08290 Cerdanyola del Vallès, Barcelona, Spain*

[g]*ICREA, Pg. Lluís Companys 23, 08010 Barcelona, Spain*

† These authors contributed equally to this work.

particular, Zr- and RE-carboxylate frameworks offer exceptional stability, which is attributed to the strong coordination bonds between high-valent metal cations and hard carboxylate ligands, consistent with Pearson's Hard and Soft Acids and Bases (HSAB) principle.[13]

To date, the combination of Zr- and RE-clusters with a variety of organic carboxylate-based linkers – mainly, ditopic, tritopic, and tetratopic linkers – has contributed significantly to the development of high-connected MOFs.[14–17] Among them, tetratopic ligands are particularly appealing, as they are intrinsically high-connected MBBs whose conformational flexibility can be tuned to expand the structural diversity of the resulting MOFs, further enriching repertoire of the reticular chemistry.

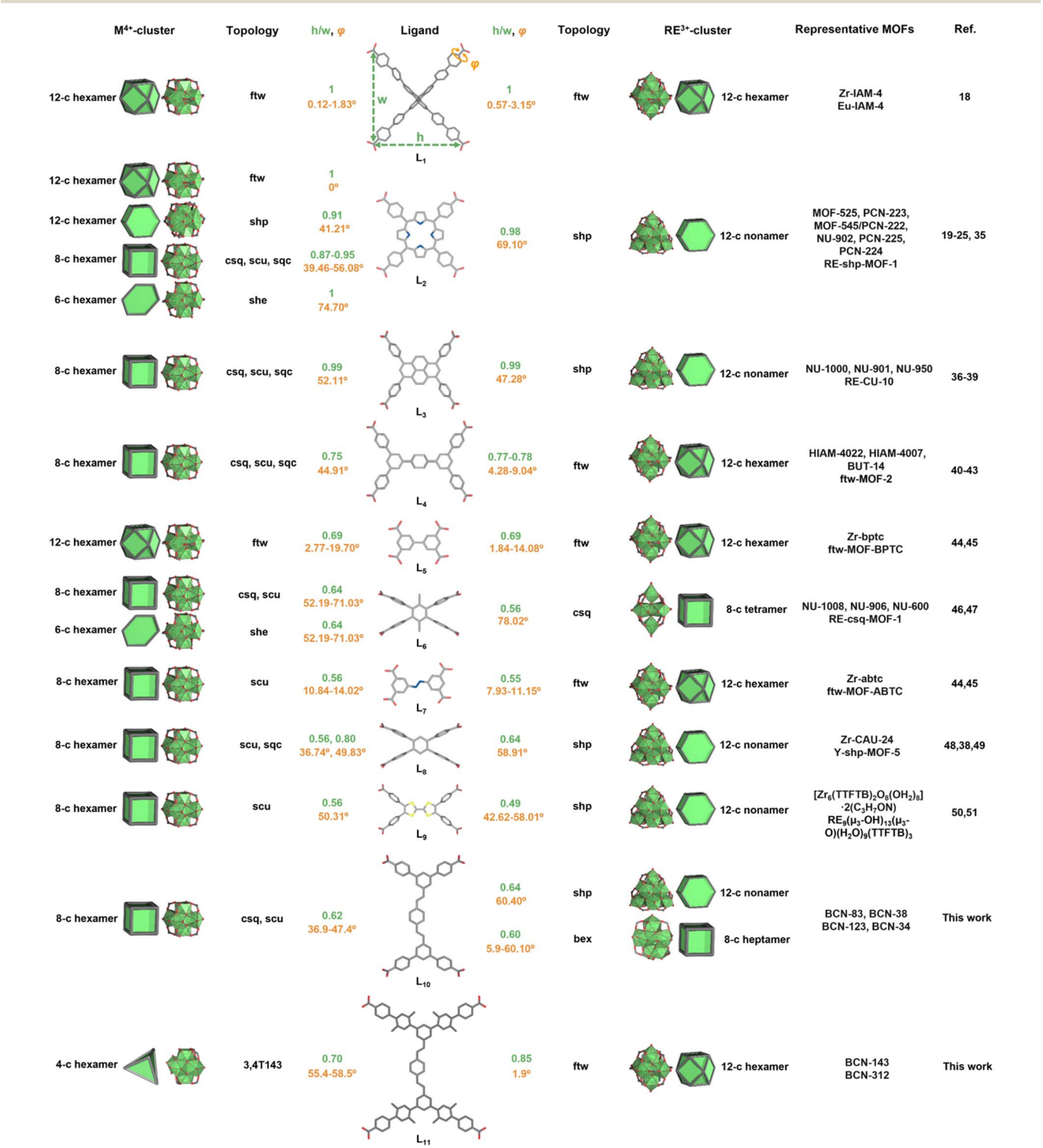


Fig. 1 Comparing the connectivity of Zr- and RE-clusters with identical 4-c square/rectangular tetratopic linkers.

For instance, connecting Zr clusters with a regular 4-connected (4-c) organic MBB, such as 4,4′,4″,4‴-(9,9′-spirobi[fluorene]-2,2′,7,7′-tetrayl)tetrakis([1,1′-biphenyl]-4′-carboxylate), typically yields a 3D MOF with the expected **ftw** topology, in which the 4-c linkers bridge archetypal 12-c Zr clusters ($L_1$ linker in Fig. 1).[18] However, when these 4-c MBBs deviate from their ideal geometry or symmetry, they can lead to MOFs with unexpected topologies and, in some cases, the formation of novel metal cluster types. A representative example is the planar tetratopic linker tetrakis(4-carboxyphenyl)porphyrin ($H_4$TCPP, $L_2$ linker in Fig. 1), which has been shown to generate diverse framework structures depending on its conformation. Note that here, planarity refers to the condition where all four carboxylate groups lie in the same geometric plane. When TCPP adopts a regular, symmetric geometry, it forms the expected (4,12)-c **ftw** topology having the expected 12-c Zr cluster. In contrast, when it adopts a less symmetric conformation – primarily due to variations in its height-to-width (*h*/*w*) ratio and/or the torsion angle ($\varphi$) between the carboxylate groups and the porphyrin core – it can connect to Zr clusters in alternative ways, enabling the formation of distinct MOFs exhibiting (4,12)-c **ftw**,[19,20] (4,12)-c **shp**,[21] (4,8)-c **csq**,[19,22] (4,8)-c **sqc**,[23] (4,8)-c **scu**[24] and (4,6)-c **she**[25] nets topologies that are formed by 12-c clusters as well as less-connected, more defective 8-c and 6-c clusters (Fig. 1).

This example perfectly illustrates the power of desymmetrising organic MBBs as a strategy to discover and access new highly connected MOFs with novel topologies that, in turn, can show different metal clusters. Although predicting the final MOF structure becomes more challenging, several research groups – including ours – have recently employed linker desymmetrisation to uncover new Zr- and RE-based MOFs.[26–34]

However, when comparing the effects of linker desymmetrisation in Zr-MOFs and RE-MOFs, some key differences emerge. In Zr-MOFs, increasing linker desymmetrisation tends to decrease the connectivity of the resulting Zr clusters. In contrast, RE clusters typically retain their connectivity even as linker desymmetrisation increases (Fig. 1).[35–51]

To investigate this behaviour further, we conducted a systematic comparison using the Cambridge Structural Database (CSD), restricting the scope to identical 4-c square/rectangular linkers used in both Zr- and RE-MOFs, and to structures exhibiting a single type of metal MBB. This analysis revealed that for Zr clusters, elongating tetratopic linkers with lower *h*/*w* ratios reduces cluster connectivity from a 12-c cuboctahedral shape to an 8-c cubic or even a 4-c square geometry (see for example, from $L_3$ to $L_9$ in Fig. 1). Additionally, we observed that for linkers with carboxylate torsion angles above 70°, the cluster connectivity drops to 6-c with a hexagonal shape, regardless of the *h*/*w* ratios of the linkers.

In contrast, RE-based clusters generally maintain their full connectivity (see also from $L_3$ to $L_9$ in Fig. 1). Only a few examples of lower-connected RE clusters have been reported, typically requiring specific linker geometries. Unlike the relatively uniform hexanuclear Zr clusters, $RE^{3+}$ clusters display greater diversity (including tetra-, hexa-, and nonanuclear clusters), making them more difficult to predict. This variability stems from the flexible coordination sphere of $RE^{3+}$ ions, which can range from six-to nine-coordinate, allowing for multiple coordination environments and enhancing cluster versatility. Furthermore, recent studies have shown the presence of bridging $\mu_3$-F species in RE-clusters. These fluoride bridges, originating from fluorinated modulators essential for RE-cluster formation, can partially or completely replace $\mu_3$-O or $\mu_3$-OH bridges; a distinctive feature compared to Zr clusters.[52–56]

Among the various RE clusters, hexanuclear and nonanuclear species are the most commonly observed, giving rise to MOFs with **ftw** and **shp** topologies, respectively. Unlike Zr-MOFs, we observed that the *h*/*w* ratio of the linker does not significantly influence cluster formation or network topology in RE-MOFs. Instead, the rotation of the carboxylate groups plays a more critical role. When the carboxylate groups are coplanar with the central core of the linker, a hexanuclear RE-cluster is favoured, leading to RE-**ftw**-MOFs. However, as reported by Howarth and co-workers, the formation of RE-**shp**-MOFs requires a torsional angle between the carboxylate groups and the central core.[39] This is likely due to the incompatibility of the hexanuclear RE-cluster with such a geometry, making the nonanuclear RE-cluster more thermodynamically favoured. This trend is clearly illustrated when comparing MOFs constructed from Zr- and RE-clusters (Fig. 1), emphasizing their distinct reactivity; a difference that has been wrongly assumed to be similar over the past decade.

Motivated by the limited number of studies systematically comparing the reactivity of desymmetrised linkers with Zr(IV) and RE(III) ions,[35,57,58] we further explored this approach using two new nanosized tetratopic linkers ($L_{10}$ and $L_{11}$), each featuring a central phenyl core with four significantly elongated carboxylic acid arms containing olefinic bonds. This design offers increased rotational flexibility and the ability to adopt multiple conformations upon coordination with Zr(IV) and RE(III) ions, potentially directing the formation of diverse clusters and MOFs with distinct topologies.

Using these two linkers, we anticipate the synthesis of three novel Zr-based MOFs: the (4,8)-c **csq** (**xly**) **BCN-83**, (4,8)-c **scu** (**tty**) **BCN-38** and (4,4)-c 3,4T143 **BCN-143**. The first two Zr-MOFs are built from 8-c Zr-clusters, supporting the trend of reduced connectivity in the presence of desymmetrised linkers. Notably, **BCN-143** features a rare, highly defective 4-c Zr cluster, which we attribute to the distortion adopted by $L_{11}$, enabling it to behave as a tetrahedral linker.

Similarly, combining both linkers with Y(III) ions (chosen as a representative RE(III) ion due to its lower cost and potential for generalisation to other RE-MOF systems),[47,59–62] led to the synthesis of three additional MOFs: (4,12)-c **shp** (**ced**) **BCN-123**, (4,8)-c 4,8L15 (3,8L19) **BCN-34** and (4,12)-c **ftw** (**kle**) **BCN-312**. As expected, two of these RE-MOFs are constructed from 12-c RE clusters. However, **BCN-34** exhibits the formation of an unprecedented 8-c heptanuclear RE cluster, attributed to the rotation of the peripheral phenyl rings of $L_{10}$, which induces a more desymmetrised configuration. These results further support the linker desymmetrisation strategy as a powerful tool to access a wide range of MOFs, including those featuring unconventional clusters and topologies.

Finally, we evaluated the reactivity of all these Zr- and RE-MOFs toward P–F bond hydrolysis of the G-type nerve agent simulant diisopropylfluorophosphate (DIFP). The results show that both the reported Zr-MOF and Y-MOF are capable of degrading this toxic compound in buffered aqueous suspensions (pH 7.4, simulating physiological conditions) as well as when impregnated onto the solid catalyst (simulating a self-cleaning adsorbent).

## Results and discussion

### Synthesis of novel Zr-MOFs

The tetratopic linker $L_{10}$ was initially prepared in high yield (>90%) through a novel synthetic route based on the well-known Wittig–Horner olefination reaction by using a phosphate and a ketone, followed by a saponification process (see SI for more details). On the other hand, linker $L_{11}$ was mainly prepared through three steps. The functional methyl groups in the peripherical arms are introduced to enhance the solubility during the linker synthesis. First, the backbone of the linker was synthesised by a Wittig–Horner reaction using phosphate and aldehyde precursors. Subsequently, the prepared peripheral arms were coupled to this backbone through a Miyaura borylation reaction. Finally, the linker $L_{11}$ was obtained *via* a saponification process (see SI for more details).

To obtain the first Zr-MOF, we carried out a solvothermal reaction between $ZrOCl_2 \cdot 8H_2O$ and $L_{10}$ in *N*,*N*-diethylformamide (DEF), using benzoic acid as the modulator, at 120 °C for 48 h. The resulting needle-like single crystals, **BCN-83**, were characterised by single-crystal X-ray diffraction (SCXRD). **BCN-83** crystallises in the hexagonal *P*6/*mmm* space group, with unit cell parameters $a = b = 39.9365(4)$ Å, $c = 24.4862(4)$ Å, and $V = 33\,821.4(9)$ Å$^3$. Its structure consists of 8-c cuboid hexanuclear clusters, $[Zr_6(\mu_3\text{-}O)_4(\mu_3\text{-}OH)_4]^{12-}$, linked by 4-c linkers $L_{10}$, forming a 3-periodic (4,8)-c framework (Fig. 2). Topologically, if $L_{10}$ is considered as a 4-c rectangular node, the underlying net corresponds to a (4,8)-c edge-transitive **csq** topology. However, considering the orientation of the tetratopic linker, $L_{10}$ can be split into two 3-c triangular nodes, leading to a (3,8)-c **xly** topology, a **csq**-derived net. The overall charged balanced chemical formula for **BCN-83** is $Zr_6(\mu_3\text{-}O)_4(\mu_3\text{-}OH)_4(H_2O)_4(OH)_4(L_{10})_2$.

Notably, Zr-MOFs built from tetratopic linkers adopting the **csq** topology have been widely reported, including the well-known NU-1000, constructed from a rectangular pyrene-core linker.[36] Similar to NU-1000, two types of 1D open channels are observed along the *c* axis: a triangular microchannel with

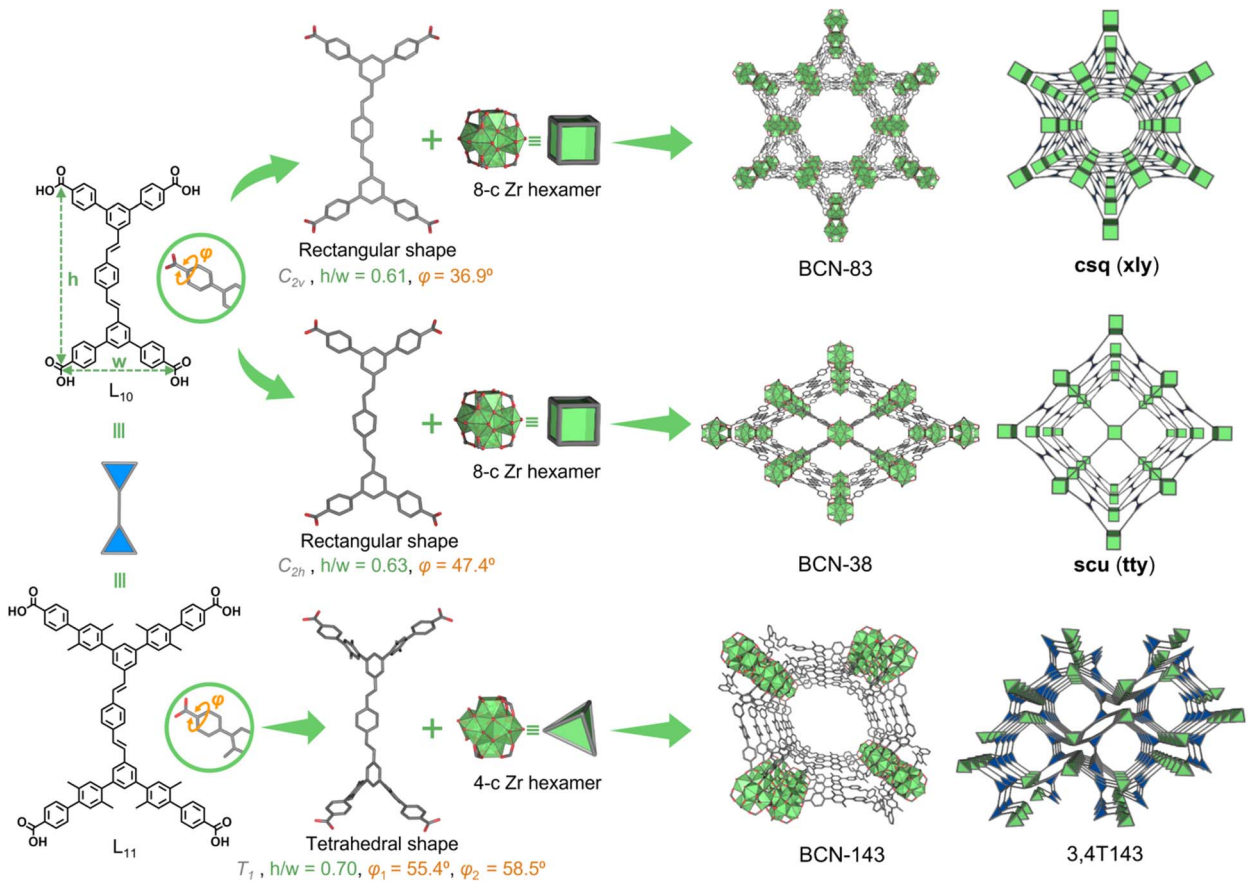


Fig. 2 Structure representation of various Zr-MOFs formed by using rectangular tetratopic linkers in this study.

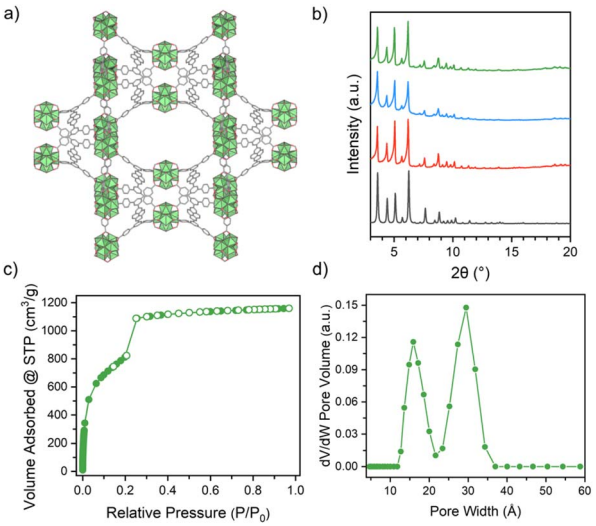


Fig. 3 (a) The structural representation of **BCN-83**; (b) PXRD patterns of simulated (black), as-made (red), acetone-exchanged (blue) and activated (green) **BCN-83**; (c) $N_2$ sorption isotherm of **BCN-83**; (d) DFT pore size distribution of **BCN-83**.

a diameter of 1.5 nm and the hexagonal mesochannel with a diameter of 3 nm (Fig. 2 and 3a). Additionally, the $L_{10}$ linkers exhibit symmetric positional disorder about an inversion center. This results in a spatial overlap between the dislocated phenylenedivinylene moiety of $L_{10}$ and a pyrene unit (Fig. S9). The refined structural model indicates site occupancy factors of 0.5. Interestingly, the linker adopts only one configuration: σ-*cis*, π-*trans*,*trans*, where the σ bond refers to the linkage between the alkene group and the central phenylene backbone.

To evaluate the porosity, **BCN-83** was soaked in acetone for two days (Fig. 3b) and then activated by supercritical carbon dioxide (sc-$CO_2$). The $N_2$ adsorption isotherm at 77 K confirmed permanent porosity, showing a fully reversible Type IV(b) isotherm with a sharp uptake at a $P/P_0$ value of 0.198, characteristic of mesoporous materials (Fig. 3c, S10). The Brunauer–Emmett–Teller surface area ($S_{BET}$) was calculated to be 2959 $m^2$ $g^{-1}$, exceeding that of NU-1000.[35] The pore size distribution (PSD), derived using density functional theory (DFT), revealed two distinct pore sizes (1.5 and 2.9 nm), in good agreement with the crystallographic data (Fig. 3d and Table S8).

Inspired by previous examples demonstrating the polymorphism of Zr-MOFs under varying synthetic conditions,[46] we also found that by altering the metal precursor, solvent, and modulator, a distinct polymorph could be obtained. Specifically, the reaction of $ZrCl_4$ with the linker $L_{10}$ in *N*,*N*-dimethylformamide (DMF), using an excess of acetic acid as a modulator, at 120 °C for 5 days, yielded spheroid-shaped crystals.

SCXRD analysis revealed that **BCN-38** crystallises in the orthorhombic space group *Cmmm* with cell parameters of $a$ = 21.1486(10) Å, $b$ = 34.1491(10) Å, $c$ = 24.7133(5) Å and $V$ = 17 848.1(11) $Å^3$. Similar to **BCN-83**, its structure consists of 8-c cuboid $[Zr_6(\mu_3\text{-}O)_4(\mu_3\text{-}OH)_4]^{12-}$ clusters linked by 4-c $L_{10}$ linkers, forming a new 3-periodic (4,8)-c framework with an edge-transitive **scu** net (Fig. 2). Considering the spatial orientation of the tetratopic ligand, the resulting underlying net corresponds to a (3,8)-c **tty** topology, a **scu**-derived net. The overall charged balanced chemical formula of **BCN-38** is $Zr_6(\mu_3\text{-}O)_4(\mu_3\text{-}OH)_4(H_2O)_4(OH)_4(L_{10})_2$.

PXRD pattern of as-made **BCN-38** showed slight deviations compared to the simulated data from the single crystal structure obtained at 100 K (Figure S11). This discrepancy may be attributed to the flexible nature of this MOF. To investigate further, we measured the single crystal structure of **BCN-38** at room temperature (RT) and successfully obtained the SCXRD data. The structure retains the same space group at 100 K with minor changes in the cell parameters and the cell volume ($a$ = 22.2811(8) Å, $b$ = 33.7528(9) Å, $c$ = 24.5977(4) Å, and $V$ = 18 498.7(9) $Å^3$), confirming the dynamic behaviour upon temperature. Interestingly, similar to previously reported **scu**-type MOFs, **BCN-38** also exhibits breathing behaviour triggered by solvents.[44] PXRD of the activated sample shows a different phase, which can be attributed to a contracted framework (Fig. S11). Upon solvation, the structure can be restored to its original state by immersing the activated sample in DMF solvent (Fig. S11). This breathing behaviour has also been confirmed by $N_2$ adsorption measurements, as the activated **BCN-38** showed to be nonporous.

Upon switching to $L_{11}$, the reaction of $ZrOCl_2 \cdot 8H_2O$ with the linker $L_{11}$ in DMF, in the presence of excess formic acid as a modulator at 120 °C for 7 days, yielded spheroid-shaped crystals, **BCN-143**. Single-crystal X-ray diffraction (SCXRD) analysis revealed that **BCN-143** crystallises in the orthorhombic space group *Pcca*, with unit cell parameters $a$ = 14.116 Å, $b$ = 18.852 Å, $c$ = 40.354 Å, and $V$ = 10 738 $Å^3$.

The structure features a rare 4-c $[Zr_6(\mu_3\text{-}O)_4(\mu_3\text{-}OH)_4]^{12-}$ cluster that adopts a previously unreported geometry within the Zr-MOF family (Fig. 2). In contrast to the symmetric square-like geometry observed in other reported 4-c Zr-cluster-based MOFs,[44,63] this cluster adopts an unprecedented tetrahedral conformation. Each 4-c Zr cluster connects to two adjacent clusters *via* two doubly bridged formate ions, resulting in a zigzag-shaped one-dimensional chain (Fig. S12). Interestingly, each cluster incorporates eight formate ions with two distinct coordination modes (Fig. S13). Four of these formates coordinate internally to Zr(IV) cations within the cluster in a typical bidentate *syn*,*syn* $\mu_2$-$\eta^1$:$\eta^1$ bridging mode. The remaining four formates, located in the equatorial plane of the cluster, bridge neighbouring clusters *via* a less common *anti*,*anti* $\mu_2$-$\eta^1$:$\eta^1$ mode.

From a topological perspective, the $Zr_6$ cluster can be regarded as a 4-c tetrahedral node, while the tetratopic $L_{11}$ ligand can be simplified into two 3-c triangular nodes. This abstraction results in a 3-periodic underlying 3,4T143 net. To the best of our knowledge, this topology is unprecedented among MOFs constructed from carboxylate-based ligands or inorganic clusters. Alternatively, if the ligand is represented as a 4-c tetrahedral node, the resulting net corresponds to a new topology.

The structure displays a two-fold interpenetrated framework featuring two distinct 1D open microchannels: a hexagonal

channel (4.10 × 5.93 Å) along the *c*-axis and a rectangular channel (3.88 × 7.58 Å) along the *a*-axis (Fig. S14, S15). The overall charge-balanced chemical formula of **BCN-143** is $Zr_6(\mu_3\text{-}O)_4(\mu_3\text{-}OH)_4(H_2O)_4(OH)_6(HCOO)_2(L_{11})$.

Prior to gas sorption measurements, **BCN-143** was activated by solvent exchange with acetone to remove residual DMF, followed by sc-$CO_2$ activation. The $N_2$ adsorption isotherm recorded at 77 K confirmed the microporosity of the framework, with a $S_{BET}$ of 425 $m^2\ g^{-1}$ (Fig. S16 and Table S8). The PSD curve shows a dominant pore centered at 5.6 Å, consistent with the crystallographic data (Fig. S17).

### Synthesis of novel RE-MOFs

To evaluate the reactivity differences between Zr-clusters and RE clusters using the same linkers $L_{10}$ and $L_{11}$, we investigated the synthesis of corresponding RE-MOFs. Initially, a mixture of $Y(NO_3)_3\cdot 6H_2O$ and the linker $L_{10}$ in DMF, using 2-fluorobenzoic acid (2-FBA) as a modulator, was heated at 120 °C for 24 h, yielding hexagonal-shaped single crystals, **BCN-123**, suitable for SCXRD analysis. SCXRD revealed that **BCN-123** crystallises in the hexagonal space group $P\bar{6}m2$ with cell parameters of $a = 22.3625(4)$ Å, $b = 22.3625(4)$ Å, $c = 24.3563(12)$ Å, and $V = 10\,548.3(6)$ $Å^3$.

The structure of **BCN-123** features an archetypal nonanuclear Y(III)-based ($Y_9$) cluster, coordinated by 12 carboxylate groups from 12 individual $L_{10}$ linkers (Fig. 4 and 5a). Topological analysis indicates that the $Y_9$ cluster can be simplified into a 12-c hexagonal prism node. This building unit, in combination with the tetratopic rectangular $L_{10}$ linker, forms a 3-periodic framework with a (4,12)-c edge-transitive **shp**

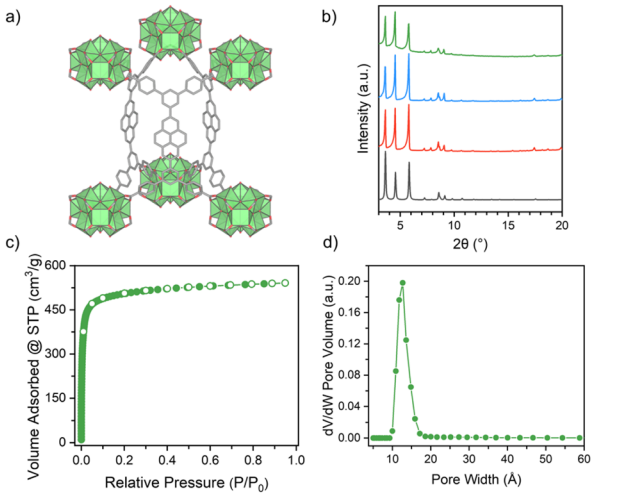


Fig. 5 (a) The structural representation of **BCN-123**; (b) PXRD patterns of simulated (black), as-made (red), acetone-exchanged (blue) and activated (green) **BCN-123**; (c) $N_2$ sorption isotherm of **BCN-123**; (d) DFT pore size distribution of **BCN-123**.

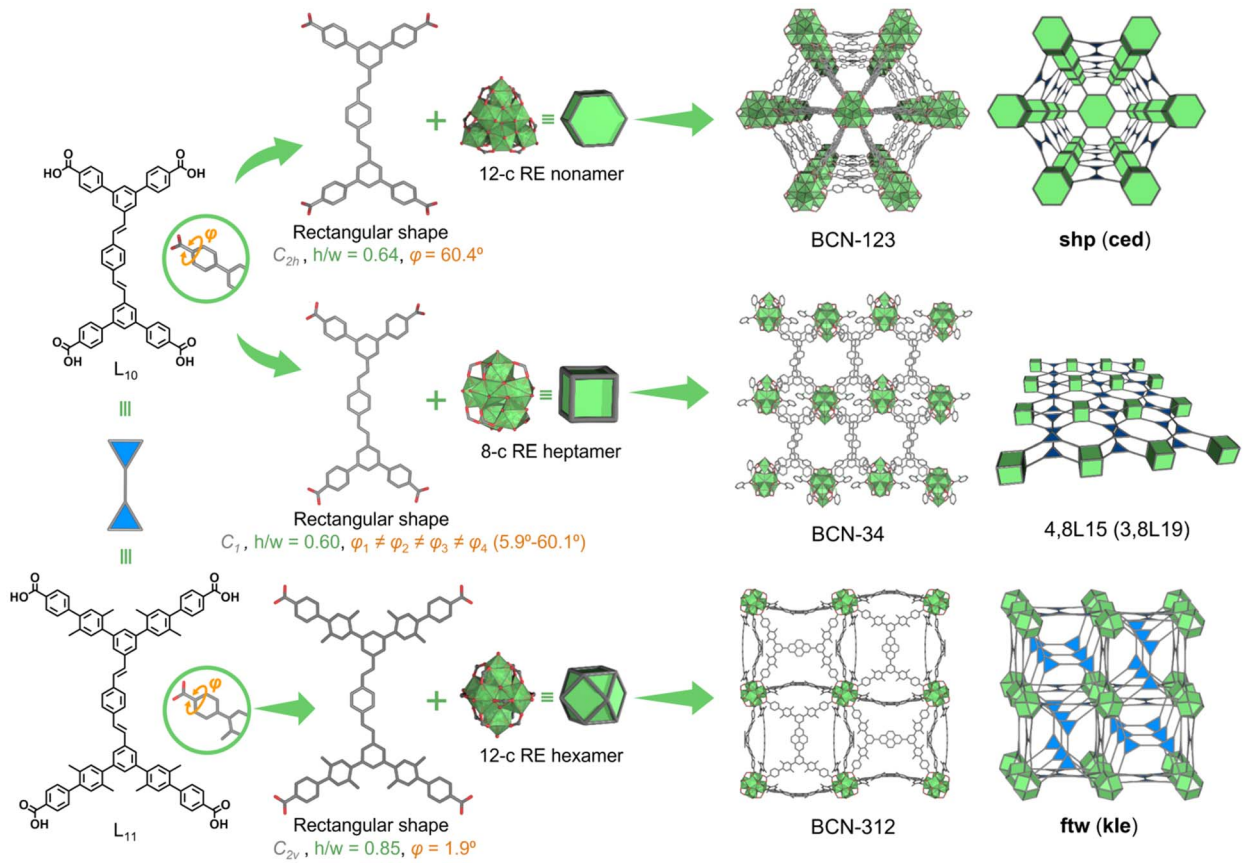


Fig. 4 Structure representation of various RE-MOFs formed by using rectangular tetratopic linkers in this study.

topology. Alternatively, the structure can also be described by the derived (3,12)-c **ced** topology. The crystalline structure of **BCN-123** contains a uniform 1D triangular channel along the *c* axis, with an approximate diameter of 11 Å, as well as hexagonal prismatic cages enclosed by two $Y_9$ clusters and six linkers, with a diameter of *ca.* 12 Å (Fig. S18).

Considering the anionic nature of $Y_9$ clusters reported in previous studies,[8,64–66] the overall charge-balanced chemical formula of **BCN-123** is $(DMA)_3[Y_9(\mu_3\text{-}O)_2(\mu_3\text{-}X)_{12}(OH)_2(L_{11})_3]$, where X = OH or F, and DMA represents dimethylammonium cation generated from the decomposition of DMF molecules. Although the presence of $\mu_3$-F bridges is difficult to confirm through crystallography, it was verified by $^{19}F$ NMR of an acid-digested sample, which showed the signal at −166 ppm, corresponding to inorganic $F^-$ anions (Fig. S19). This observation is consistent with the presence of fluoro-bridged clusters, in agreement with previous reports.[31,67]

To evaluate its porosity properties, **BCN-123** was first activated by exchanging DMF with acetone (Fig. 5b) as a volatile solvent, followed by sc-$CO_2$ treatment. The reversible type I $N_2$ adsorption isotherm at 77 K confirmed the permanent porosity of **BCN-123**. The $S_{BET}$ surface area was calculated to be 2030 $m^2 g^{-1}$, which is higher than that of previously reported RE-**shp**-MOFs (Fig. 5c, S20 and Table S8).[39] The PSD curve exhibits a main peak centered at 12 Å, consistent with the crystallographic analysis (Fig. 5d).

It is well known that in certain cases, the use of co-modulators is crucial for the synthesis of RE-MOFs; not only for obtaining high-quality single crystals but also for improving yield.[62,68] In our efforts to crystallise **BCN-123**, we explored a variety of co-modulators, including fluorinated modulators (2-FBA or 2,6-dFBA) as well as others such as water, $HNO_3$, and acetic acid. This exploration unexpectedly led to the discovery of a new RE-MOF phase, **BCN-34**.

**BCN-34** was synthesised by combining $Y(NO_3)_3 \cdot 6H_2O$ and the linker $L_{10}$ in DMF, using 2-FBA and $HNO_3$ as co-modulators, and heating the mixture at 120 °C for 7 days. The introduction of $HNO_3$ increased the acidity of the reaction medium, which slowed down the crystallisation process and ultimately yielded rod-shaped single crystals of **BCN-34**.

SCXRD analysis revealed that **BCN-34** crystallises in the orthorhombic space group *Pnma*, with unit cell parameters $a$ = 14.4620(10) Å, $b$ = 35.446(2) Å, and $c$ = 26.498(2) Å. The asymmetric unit contains seven crystallographically independent $Y^{3+}$ cations, two coordinated tetratopic $L_{10}$ linkers, eight $\mu_3$-X groups and one $\mu_2$-X group, four coordinated 2-FBA anions, and six terminal water molecules.

These seven Y(III) centers exhibit coordination numbers ranging from 7 to 9, with distinct coordination environments: Y1 and Y2 are 8-coordinate, each bonded to four $\mu_3$-X groups and four oxygen atoms (two from $L_{10}$ and two from 2-FBA anions); Y3 and Y4, also 8-coordinate, are each coordinated by four $\mu_3$-X groups, two oxygen atoms from two $L_{10}$, one 2-FBA anion, and one water molecule; Y5 is 8-coordinate as well, coordinated by three $\mu_3$-X groups, two oxygen atoms from $L_{10}$, one $\mu_2$-X group, and two water molecules; Y6 is 7-coordinate, bonded to one $\mu_3$-X, one $\mu_2$-X, two oxygen atoms from $L_{10}$, two 2-FBA anions, and one water molecule; and Y7 is 9-coordinate, bonded to four $\mu_3$-X groups, one $\mu_2$-X group, and four oxygen atoms from four $L_{10}$ linkers.

Interestingly, the spatial arrangement of the terminal 2-FBA anions and the carboxylate groups within the cluster is unusual: all four 2-FBA anions reside in the equatorial plane, while the eight carboxylates from eight individual ligands point upward and downward, forming an 8-c cuboid secondary building unit.

Remarkably, **BCN-34** features a previously unreported heptanuclear cluster, with the core formula $Y_7(\mu_2\text{-}X)(\mu_3\text{-}X)_8$ (Fig. 4). To date, only a limited number of structural motifs have been reported for heptanuclear RE clusters, primarily exhibiting trigonal prismatic or trigonal antiprismatic geometries.[64–72] However, the metal–oxo cluster in this study introduces a new monocapped octahedral geometry (Fig. S21), which, to the best of our knowledge, represents the first example of this type within the RE-MOF family.

In the structure of **BCN-34**, each $Y_7$ cluster is rotated 180° relative to its nearest neighbour, resulting in an alternating arrangement of clusters along the *a*-axis (Fig. S22). **BCN-34** exhibits an overall two-periodic structure, in which each $L_{10}$ linker connects to four Y(III)-based clusters, and each cluster is coordinated by eight $L_{10}$ linkers (Fig. 4). Due to the spatial configuration of the eight connection points, double cross-linking occurs *via* pairs of $L_{10}$ linkers, effectively reducing the net connectivity to four.

Topological analysis indicates that the $Y_7$ cluster can be simplified as a 8-c node, and the tetratopic $L_{10}$ linker can likewise be treated as a 4-c node. This connectivity results in a 2-periodic edge-transitive 4,8L15 net. Alternatively, the structure can be described by the derived (3,8)-c 3,8L19 topology. These nets can be regarded as the daughter nets when splitting a vertex of the parent **sql-b** or **bex** net, respectively.[73] Notably, although the 4,8L15/3,8L19 topology formed by reduced-symmetry linkers has been previously observed in Zr-MOFs,[74] it is reported here for the first time in a polynuclear RE-MOF.

The lamellar packing of **BCN-34** reveals that the two periodic layers are arranged in an *AB*-staggered configuration, with clusters occupying the voids between neighbouring layers (Fig. S23, S24). The interlayer distance resulting from π–π stacking was estimated to be 3.5 Å. This stacking arrangement produces a porous framework with 1D open quadrilateral channels (*ca.* 7 × 10 Å) along the *a*-axis.

The presence of coordinated 2-FBA anions was confirmed by both $^1H$ NMR and $^{19}F$ NMR spectroscopy of acid-digested samples (Fig. S25 and S26). The $^1H$ NMR spectrum confirmed a 1 : 2 ratio between the $L_{10}$ linker and 2-FBA, in agreement with the expected stoichiometry. Additionally, the $^{19}F$ NMR spectrum identified the presence of bridging $\mu_3$-F species, with a chemical shift at $\delta$ = −110 ppm corresponding to 2-FBA, and a signal at $\delta$ = −166 ppm attributed to inorganic $F^-$ anions.

The framework was confirmed to be neutral, as verified by inductively coupled plasma (ICP) analysis performed on a $Li^+$-exchanged, digested sample. The overall charge-balanced formula of **BCN-34** is $Y_7(\mu_2\text{-}X)(\mu_3\text{-}X)_8(H_2O)_4(2\text{-}FBA)_4(L_{10})_2$.

To measure its porous properties, **BCN-34** was activated by exchanging DMF with methanol as a volatile solvent, followed

by sc-$CO_2$ activation. The nitrogen adsorption isotherm recorded at 77 K confirmed the microporosity of **BCN-34**, with a $S_{BET}$ of 400 $m^2\ g^{-1}$ (Fig. S27 and Table S8). The PSD curve exhibited distinct peaks centered at 6.6 Å and 11 Å, in agreement with the crystallographic analysis (Fig. S28).

Finally, we explored the synthesis of a RE-MOF using the extended tetratopic linker $L_{11}$. The resulting material, **BCN-312**, was synthesised by mixing $L_{11}$, 2-FBA, and $Y(NO_3)_3 \cdot 6H_2O$, followed by heating at 120 °C for 24 h. Cubic-shaped crystals were obtained; however, SCXRD data revealed weak diffraction intensities at high angles. This may be attributed to crystal instability upon solvent loss, leading to loss of long-range order or significant structural disorder.

Further attempts to improve the crystal quality, which included the use of alternative metal sources such as $Tb(NO_3)_3 \cdot 5H_2O$, or stronger fluorinated modulators such a 2,6-dFBA, TFA, also yielded cubic single crystals. Nevertheless, the diffraction data remained low-resolution, indicating inherent structural fragility.

To elucidate the atomic structure, a model was constructed using the Materials Studio 2023 software package[75] based on a polynuclear RE-cluster. After evaluating the space group and unit cell parameters obtained from SCXRD data, possible framework topologies were explored. A 3-periodic **ftw**-type MOF model with a rectangular, planar ligand conformation was selected and geometrically optimised, using the reported Y-**ftw**-MOF-3 (CCDC 1050064) as a structural template.[43]

High-quality PXRD data for refinement were collected using synchrotron radiation (ALBA, BL13-XALOC). A comparison between the experimental and simulated patterns of the optimised structure showed excellent agreement, and Pawley refinement yielded satisfactory residuals ($R_p$ = 1.58%, $R_{wp}$ = 2.68%) for a cubic $Im\bar{3}$ space group with a unit cell parameter of 55.99(3) Å (Fig. S29 and Table S7). Topological analysis identified the simulated network as a (3,12)-c **kle** topology, a **ftw**-derived net.

According to the simulated structure, **BCN-312** is composed of the archetypal hexanuclear Y-cluster with a core of $[Y_6(\mu_3\text{-}X)_8]^{10+}$ (Fig. 4). Each $L_{11}$ linker bridges four Y-based clusters, while each cluster connects to twelve $L_{11}$ linkers. The charge-balanced formula is $(DMA)_2[Y_6(\mu_3\text{-}X)_8(L_{11})_3]$. Here, the presence of $\mu_3$-F species was confirmed by $^{19}F$ NMR, showing a single signal at $\delta = -166$ ppm, corresponding to inorganic F anions (Fig. S30).

After activation of **BCN-312** using sc-$CO_2$, $N_2$ adsorption measurement at 77 K confirmed the microporosity of **BCN-312**, with a moderate $S_{BET}$ of 722 $m^2\ g^{-1}$ (Fig. S31 and Table S8), suggesting partial framework instability. The PSD curve exhibited two main peaks centered at 7.3 Å and 12.1 Å, consistent with the crystallographic data (Fig. S32).

### Effect of linker desymmetrisation on the connectivity of Zr- and RE-clusters in MOFs derived from $L_{10}$ and $L_{11}$

In this study, the new tetratopic linker $L_{10}$ adopts a rectangular geometry and can be considered a desymmetrised variant of square-shaped ligands with $D_{4h}$ symmetry, characterised by a decreased $h/w$ ratio and an in-plane shift of the double bonds. The formation of Zr-MOFs with **ftw** topology typically requires highly symmetrical, square-shaped linkers with $D_{4h}$ symmetry. In such configurations, the torsion angle between the terminal carboxylates and the central backbone is strongly constrained to 0°, a condition that is completely disrupted in the case of $L_{10}$.

When the planar linker exhibits reduced symmetry ($C_{2h}$ or $C_{2v}$), it tends to promote the formation of MOFs featuring cuboid-like $Zr_6$ clusters. This desymmetrisation can therefore facilitate the formation of edge-transitive **csq**, **sqc**, **scu**, and **shp** topologies. Indeed, this desymmetrised linker leads to the formation of **BCN-38** and **BCN-83**, which adopt **scu** and **csq** topologies, respectively. In **BCN-38**, the $L_{10}$ linker adopts $C_{2h}$ symmetry, with twisted peripheral benzoate arms and a central phenylene unit that exhibits significant bending. The torsion angle between the carboxylate groups and the central core is 47.4°. When the linker adopts a configuration closer to $C_{2v}$ symmetry, the MOF tends to form the **csq** net, as exemplified by **BCN-83**. In this case, the torsion angle is 36.9°, and the overall dihedral angle between adjacent arms of the linker is 120.1°. Notably, the ligand metrics observed for **BCN-38** and **BCN-83** fall in the domain characteristic of **scu** and **csq** nets, consistent with our theoretical findings (Fig. S34).

These results suggest that additional phases could potentially be obtained through systematic screening of different synthetic conditions; with the notable exception of the **ftw**-based MOF phase.

In the case of RE-MOFs, the formation of **ftw** topologies typically requires linkers with planar carboxylates; otherwise, **shp** nets based on nonanuclear clusters are favoured. This trend is confirmed in **BCN-123**, where the $L_{10}$ linker adopts a reduced $C_{2h}$ symmetry with carboxylate torsion angles of 60.4°. Interestingly, a polymorph, **BCN-34**, was also isolated. In **BCN-34**, two crystallographically distinct linkers are present, both with an aspect ratio of 0.60 and four differentially oriented carboxylate groups. One carboxylate is coplanar with the central core, while the others are rotated at angles ranging from 42.25° to 61.29°. The resulting 4,8L15 net likely arises from the desymmetrisation of the linker adopting $C_1$ symmetry, similar to a previously reported Zr-MOF with the same topology and double-bridged linkers.[74] We propose that the formation of the new heptanuclear cluster in **BCN-34** is driven by the rotational flexibility of the carboxylate groups, which hinders the assembly of the canonical $RE_6$ cluster.

Most importantly, by introducing specific conformational constraints, the tetratopic linker $L_{11}$ can adopt a tetrahedral geometry, achieving the highest possible symmetry ($T_d$) among all tetratopic linkers. When the linker adopts this tetrahedral conformation, three edge-transitive nets are theoretically expected: (4,12)-c **ith**,[76] (4,8)-c **flu**,[77] and (4,6)-c **gar**.[78] Among these, the **flu** net is the most commonly observed with tetratopic linkers displaying $T_{2d}$ symmetry, whereas the **ith** net requires a distorted cluster with an icosahedral geometry. Tetratopic linkers capable of adopting tetrahedral conformations typically contain $sp^3$-hybridised carbon or nitrogen atoms, or bulky groups within their backbones.[79,80]

However, further elongation of tetrahedral linkers can result in alternative topologies, as demonstrated in studies involving linkers containing $sp^3$-carbon atoms.[81] Similarly, compared to tetratopic linkers with a biphenyl core, which often give rise to **flu** topologies,[26,82] additional desymmetrisation and a significant decrease in the aspect ratio have led to the discovery of a new net, 3,4T143, in Zr-MOFs. This net is observed in **BCN-143**, where the conformational flexibility of the central double bond units allows the ligand to adopt a distorted tetrahedral geometry ($T_1$ symmetry). The angles between two adjacent arms – measured as the angle between the carbon atoms of two carboxylate groups and the center of the tetrahedron – are approximately 79°, 116°, 128°, and 132°, deviating from the ideal tetrahedral angle of 109.47°. This distortion, along with the elongation of the arms, gives the linker an aspect ratio of 0.70. The formation of this topology is driven by the strong desymmetrisation induced by the $L_{11}$ linker, which significantly reduces the connectivity of the Zr cluster in an unconventional manner. We propose that the tetrahedral-shaped $L_{11}$ linker in **BCN-143**, stabilised by the presence of two central double bonds, primarily adopts this geometry due to the rotation of its carboxylate groups ($\varphi_1 = 55.4°$, $\varphi_2 = 58.5°$), a rotation enforced by steric hindrance from methyl groups on the arms.

In contrast, replacing the Zr cluster with its RE analogue does not result in a similar decrease in connectivity. The incorporation of methyl groups in the peripheral phenylene rings of $L_{11}$ significantly increases steric hindrance, inducing a rotation angle of 60.6° relative to the central plane of the linker. However, this steric effect also allows the four benzoate arms to align and remain nearly coplanar with the ligand core ($\varphi \approx 1.9°$), a condition necessary for forming the **ftw** net with a hexanuclear RE cluster. This structural arrangement is supported by a structural model, which show excellent agreement between the experimental and simulated PXRD patterns of **BCN-312**.

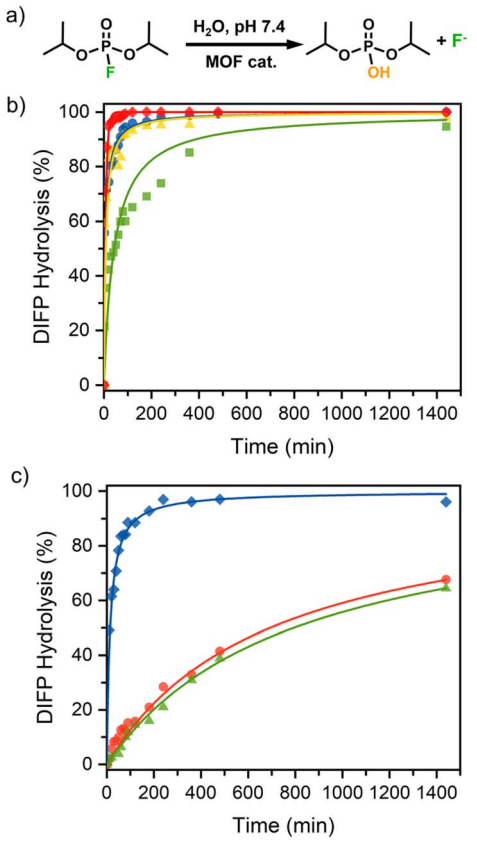


Fig. 6 (a) Schematic DIFP hydrolytic breakdown into nontoxic diisopropylphosphate (DIP). (b) Profiles of DIFP (0.015 mmol, 0.5 mL $H_2O$) hydrolytic degradation under simulated biological conditions (Tris–HCl, 0.1 M, pH = 7.4) by a suspension of the studied Zr-MOFs (0.015 mmol): **BCN-83** (red), **BCN-38** (blue), NU-1000 (yellow) and **BCN-143** (green). (c) Profiles of DIFP (0.015 mmol, 0.5 mL buffered solution) hydrolytic degradation under simulated biological conditions (Tris–HCl, 0.1 M, pH = 7.4) by a suspension of the studied RE-MOFs (0.015 mmol): **BCN-123** (red), **BCN-34** (blue), and **BCN-312** (green).

### Detoxification properties towards G-type nerve agent model

Taking into account the high Lewis acidity of Zr(IV) and Y(III) and basicity of oxide residues in Zr/RE-clusters, we evaluated the impact of framework topology on the reactivity of these materials toward P–F bond hydrolysis of the G-type nerve agent simulant diisopropylfluorophosphate (DIFP, Fig. 6a).[34,83–86] The results show that the reported Zr-MOF materials are capable of degrading this toxic compound both in buffered aqueous suspensions (pH 7.4, simulating physiological conditions) and upon surface impregnation of the solid material (RH 50%, simulating a self-cleaning adsorbent).

A 1 : 1 reaction between **BCN-83** and DIFP under simulated physiological conditions leads to the formation of the non-toxic product diisopropylphosphate (DIP), with a remarkably low half-life of 1.3 minutes (Fig. 6b, S35, S36, and Table S9). Recyclability tests of **BCN-83** demonstrated that this material is still active for DIFP degradation after four cycles (Fig. S37). For comparison purposes, the benchmark NU-1000, which features an isoreticular **csq** topology, exhibits a half-life of 7.7 minutes. **BCN-38**, featuring a **scu** topology, shows a half-life of 6.8 minutes, while **BCN-143** with a 3,4T143 topology performs more poorly, with a half-life of 55 minutes.

A similar trend is observed in the surface impregnation tests, which simulate application in protective garments or filters (Table S10). Again, the best performance is achieved by **BCN-83**, whose highly accessible pore structure enables nearly quantitative degradation (94%) after 24 hours of exposure at 30 °C and approximately 50% relative humidity. In contrast, **BCN-38**, **BCN-143**, and the benchmark NU-1000 show lower efficiencies, achieving 74%, 73%, and 45% degradation, respectively, under the same conditions. The superior performance of **BCN-83** is likely related to an optimal combination of increased accessibility to the $Zr_6$ clusters and structural robustness.

Similarly, the reported Y-MOF materials demonstrate the ability to degrade DIFP under buffered aqueous conditions (pH 7.4). A 1 : 1 reaction of DIFP with **BCN-34**, **BCN-123**, and **BCN-312** leads to the formation of DIP, with respective half-lives of 35.5, 693, and 793 minutes (Fig. 6c, S38, and Table S11). The enhanced performance of **BCN-34** is likely due to its layered 4,8L15 topology, which favours improved accessibility to the reactive $Y_7$ clusters. The lower acidity of Y-MOFs in comparison

to Zr-MOFs can be related to the lower Lewis acidity of Y(III) in comparison to Zr(IV) ions.[87]

## Conclusions

In conclusion, this work demonstrates the power of linker desymmetrisation as a strategic tool to modulate cluster connectivity in MOFs. By carefully tuning geometric features such as the height-to-width ratio and torsion angles, we have accessed a diverse set of Zr- and RE-MOFs featuring both conventional and unconventional cluster connectivities and topologies. Beyond structural diversity, we show that cluster accessibility – enabled by appropriate ligand design and pore architecture – plays a critical role in enhancing catalytic performance, as exemplified by the efficient P–F bond hydrolysis of G-type nerve agent simulants. These findings pave the way for the rational design of next-generation MOFs that combine structural precision with functional reactivity, particularly in applications requiring controlled molecular access to reactive metal sites.

## Author contributions

B. O.-R. and Y. Y. contributed equally and agree that the order of their names may be exchanged as useful to highlight their contributions in individual professional pursuits. B. O.-R., Y. Y., I. I. and D. M. conceived the idea of the project. B. O.-R. and Y. Y. designed, synthesised, and characterised the metal–organic materials. E. B.-M. and J. A. R. N. performed catalytic reactions and integrated the data. J. R.-B. and C. V. synthesised and characterised the organic linkers. I. I. and J. J. performed the SCXRD analysis and solved the structures. B. O.-R., Y. Y., and D. M. wrote the manuscript. All authors contributed to the revision of the manuscript.

## Conflicts of interest

There are no conflicts to declare.

## Data availability

Additional data are available from the corresponding authors upon reasonable request.

CCDC 2470518–2470522 and 2472930 contain the supplementary crystallographic data for this paper.[88a–f]

The data supporting this article have been included as part of the supplementary information (SI). Adsorption data have been deposited as .aif files as SI. Supplementary information: general methods, experimental procedures, NMR spectra, crystallographic tables. See DOI: **https://doi.org/10.1039/d5sc05365j**.

## Acknowledgements

This work has received funding from the European Union's Horizon 2020 research and innovation programme under grant agreement no. 101019003, Grant Ref. PID2021-124804NB-I00 funded by MCIN/AEI/10.13039/501100011033/and by "ERDF A way of making Europe", ALBA beamtime access granted through proposal ID 20250330096, and the Catalan AGAUR (project 2021 SGR 00458). It was also funded by the CERCA Program/Generalitat de Catalunya. ICN2 is supported by the Severo Ochoa Centres of Excellence Programme, Grant CEX2021-001214-S, funded by MCIN/AEI/10.13039.501100011033. E. B.-M. acknowledges the Spanish Ministry of Education for a predoctoral fellowship (FPU23/01844). J. R.-B. thanks the Ministerio de Ciencia, Innovación y Universidades for a FPU predoctoral contract (FPU17/00688, FPU23/91844). C. V. thanks the RyC contract (RYC-2016-20187) funded by MCIN/AEI/10.13039/501100011033 and by "European Union NextGenerationEU/PRTR". Y. Y. acknowledges the China Scholarship Council for scholarship support. B. O.-R. acknowledges a postdoctoral scholarship from the Max Planck Society and the European Union's Horizon Europe research and innovation programme for the receipt of a Marie Skłodowska-Curie Actions Postdoctoral Fellowship (Grant Agreement No. 101208213, MUVCATMOF, HORIZON-MSCA-2024-PF-01-01).

## Notes and references

1 O. M. Yaghi, M. J. Kalmutzki and C. S. Diercks, *Introduction to Reticular Chemistry: Metal-Organic Frameworks and Covalent Organic Frameworks*, John Wiley & Sons, 2019.
2 O. M. Yaghi, M. O'Keeffe, N. W. Ockwig, H. K. Chae, M. Eddaoudi and J. Kim, Reticular synthesis and the design of new materials, *Nature*, 2003, **423**, 705–714.
3 M. J. Kalmutzki, N. Hanikel and O. M. Yaghi, Secondary building units as the turning point in the development of the reticular chemistry of MOFs, *Sci. Adv.*, 2018, **4**, eaat9180.
4 Z. Ji, H. Z. Wang, S. Canossa, S. Wuttke and O. M. Yaghi, Pore Chemistry of Metal-Organic Frameworks, *Adv. Funct. Mater.*, 2020, **30**, 2000238.
5 R. Freund, O. Zaremba, M. Dinca, G. Arnauts, R. Ameloot, G. Skorupskii, A. Bavykina, J. Gascon, A. Ejsmont, J. Goscianska, M. Kalmutzki, U. Lächelt, E. Ploetz, C. S. Diercks and S. Wuttke, The Current Status of MOF and COF Applications, *Angew. Chem., Int. Ed.*, 2021, **60**, 23975–24001.
6 T. He, X. J. Kong and J. R. Li, Chemically Stable Metal-Organic Frameworks: Rational Construction and Application Expansion, *Acc. Chem. Res.*, 2021, **54**, 3083–3094.
7 V. Guillerm and M. Eddaoudi, The Importance of Highly Connected Building Units in Reticular Chemistry: Thoughtful Design of Metal-Organic Frameworks, *Acc. Chem. Res.*, 2021, **54**, 3298–3312.
8 D. Alezi, A. M. P. Peedikakkal, L. J. Weselinski, V. Guillerm, Y. Belmabkhout, A. J. Cairns, Z. J. Chen, L. Wojtas and M. Eddaoudi, Quest for Highly Connected Metal-Organic Framework Platforms: Rare-Earth Polynuclear Clusters Versatility Meets Net Topology Needs, *J. Am. Chem. Soc.*, 2015, **137**, 5421–5430.
9 F. Nouar, J. F. Eubank, T. Bousquet, L. Wojtas, M. J. Zaworotko and M. Eddaoudi, Supermolecular Building Blocks (SBBs) for the Design and Synthesis of

Highly Porous Metal-Organic Frameworks, *J. Am. Chem. Soc.*, 2008, **130**, 1833–1835.

10 J. F. Eubank, H. Mouttaki, A. J. Cairns, Y. Belmabkhout, L. Wojtas, R. Luebke, M. Alkordi and M. Eddaoudi, The Quest for Modular Nanocages: tbo-MOF as an Archetype for Mutual Substitution, Functionalization, and Expansion of Quadrangular Pillar Building Blocks, *J. Am. Chem. Soc.*, 2011, **133**, 14204–14207.

11 J. H. Cavka, S. Jakobsen, U. Olsbye, N. Guillou, C. Lamberti, S. Bordiga and K. P. Lillerud, A new zirconium inorganic building brick forming metal organic frameworks with exceptional stability, *J. Am. Chem. Soc.*, 2008, **130**, 13850–13851.

12 D. X. Xue, A. J. Cairns, Y. Belmabkhout, L. Wojtas, Y. L. Liu, M. H. Alkordi and M. Eddaoudi, Tunable Rare-Earth fcu-MOFs: A Platform for Systematic Enhancement of $CO_2$ Adsorption Energetics and Uptake, *J. Am. Chem. Soc.*, 2013, **135**, 7660–7667.

13 R. G. Pearson, Hard and Soft Acids and Bases, *J. Am. Chem. Soc.*, 1963, **85**, 3533–3539.

14 Z. Chen, S. L. Hanna, L. R. Redfern, D. Alezi, T. Islamoglu and O. K. Farha, Reticular chemistry in the rational synthesis of functional zirconium cluster-based MOFs, *Coord. Chem. Rev.*, 2019, **386**, 32–49.

15 L. Shi, Z. N. Yang, F. R. Sha and Z. J. Chen, Design, synthesis and applications of functional zirconium-based metal-organic frameworks, *Sci. China Chem.*, 2023, **66**, 3383–3397.

16 F. Saraci, V. Quezada-Novoa, P. R. Donnarumma and A. J. Howarth, Rare-earth metal-organic frameworks: from structure to applications, *Chem. Soc. Rev.*, 2020, **49**, 7949–7977.

17 O. V. Gutov, W. Bury, D. A. Gomez-Gualdron, V. Krungleviciute, D. Fairen-Jimenez, J. E. Mondloch, A. A. Sargent, S. S. Al-Juaid, R. Q. Snurr, J. T. Hupp, T. Yildirim and O. K. Farha, Water-Stable Zirconium-Based Metal–Organic Framework Material with High-Surface Area and Gas-Storage Capacities, *Chem.–Eur. J.*, 2014, **20**(39), 12389–12393.

18 Z. Duan, Y. Li, X. Xiao, X. Huang, X. Li, Y. Li, C. Zhang, H. Zhang, L. Li, Z. Li, Y. Zhao and W. Huang, Interpenetrated Metal–Organic Frameworks with ftw Topology and Versatile Functions, *ACS Appl. Mater. Interfaces*, 2020, **12**(16), 18715–18722.

19 W. Morris, B. Volosskiy, S. Demir, F. Gándara, P. L. McGrier, H. Furukawa, D. Cascio, J. F. Stoddart and O. M. Yaghi, Synthesis, Structure, and Metalation of Two New Highly Porous Zirconium Metal-Organic Frameworks, *Inorg. Chem.*, 2012, **51**, 6443–6445.

20 C. Koschnick, R. Stäglich, T. Scholz, M. W. Terban, A. von Mankowski, G. Savasci, F. Binder, A. Schökel, M. Etter, J. Nuss, R. Siegel, L. S. Germann, C. Ochsenfeld, R. E. Dinnebier, K. Senker and B. V. Lotsch, Understanding disorder and linker deficiency in porphyrinic zirconium-based metal–organic frameworks by resolving the $Zr_8O_6$ cluster conundrum in PCN-221, *Nat. Commun.*, 2021, **12**, 3099.

21 D. W. Feng, Z. Y. Gu, Y. P. Chen, J. Park, Z. W. Wei, Y. J. Sun, M. Bosch, S. Yuan and H. C. Zhou, A Highly Stable Porphyrinic Zirconium Metal-Organic Framework with shp-a Topology, *J. Am. Chem. Soc.*, 2014, **136**, 17714–17717.

22 D. W. Feng, Z. Y. Gu, J. R. Li, H. L. Jiang, Z. W. Wei and H. C. Zhou, Zirconium-Metalloporphyrin PCN-222: Mesoporous Metal-Organic Frameworks with Ultrahigh Stability as Biomimetic Catalysts, *Angew. Chem., Int. Ed.*, 2012, **51**, 10307–10310.

23 H. L. Jiang, D. W. Feng, K. C. Wang, Z. Y. Gu, Z. W. Wei, Y. P. Chen and H. C. Zhou, An Exceptionally Stable, Porphyrinic Zr Metal-Organic Framework Exhibiting pH-Dependent Fluorescence, *J. Am. Chem. Soc.*, 2013, **135**, 13934–13938.

24 P. Deria, D. A. Gómez-Gualdrón, I. Hod, R. Q. Snurr, J. T. Hupp and O. K. Farha, Framework-Topology-Dependent Catalytic Activity of Zirconium-Based (Porphinato)zinc(II) MOFs, *J. Am. Chem. Soc.*, 2016, **138**, 14449–14457.

25 D. W. Feng, W. C. Chung, Z. W. Wei, Z. Y. Gu, H. L. Jiang, Y. P. Chen, D. J. Darensbourg and H. C. Zhou, Construction of Ultrastable Porphyrin Zr Metal-Organic Frameworks through Linker Elimination, *J. Am. Chem. Soc.*, 2013, **135**, 17105–17110.

26 J. Ma, L. D. Tran and A. J. Matzger, Toward Topology Prediction in Zr-Based Microporous Coordination Polymers: The Role of Linker Geometry and Flexibility, *Cryst. Growth Des.*, 2016, **16**(7), 4148–4153.

27 L. Feng, Y. Wang, K. Zhang, K.-Y. Wang, W. Fan, X. Wang, J. A. Powell, B. Guo, F. Dai, L. Zhang, R. Wang, D. Sun and H.-C. Zhou, Molecular Pivot-Hinge Installation to Evolve Topology in Rare-Earth Metal–Organic Frameworks, *Angew. Chem., Int. Ed.*, 2019, **46**, 16682–16690.

28 Y. Wang, L. Feng, K. Zhang, K.-Y. Wang, W. Fan, X. Wang, B. Guo, F. Dai, L. Zhang, D. Sun and H.-C. Zhou, Uncovering Structural Opportunities for Zirconium Metal-Organic Frameworks via Linker Desymmetrization, *Adv. Sci.*, 2019, **23**, 1901855.

29 X.-L. Lv, L. Feng, L.-H. Xie, T. He, W. Wu, K.-Y. Wang, G. Si, B. Wang, J.-R. Li and H.-C. Zhou, Linker Desymmetrization: Access to a Series of Rare-Earth Tetracarboxylate Frameworks with Eight-Connected Hexanuclear Nodes, *J. Am. Chem. Soc.*, 2021, **143**, 2784–2791.

30 Y. Chen, H. Xie, X. Wang, F. Sha, K. O. Kirlikovali, X. Wang, Z.-M. Ye, X. Tang, C. Zhang, G. W. Peterson, Z. Li and O. K. Farha, Leveraging Ligand Desymmetrization to Enrich Structural Diversity of Zirconium Metal–Organic Frameworks for Toxic Chemical Adsorption, *Angew. Chem., Int. Ed.*, 2024, **5**, e202417664.

31 E. Loukopoulos, C. Tsangarakis, K. G. Froudas, M. Vassaki, G. K. Angeli and P. N. Trikalitis, Accessing mixed cluster rare-earth MOFs with reduced connectivity *via* linker expansion and desymmetrization: co-assembly of 6-c and 10-c hexanuclear clusters in RE-stc-MOF-1, *J. Mater. Chem. C*, 2025, **13**, 31–36.

32 W. Han, X. Ma, J. Wang, F. Leng, C. Xie and H.-L. Jiang, Endowing Porphyrinic Metal–Organic Frameworks with

High Stability by a Linker Desymmetrization Strategy, *J. Am. Chem. Soc.*, 2023, **145**, 9665–9671.

33 C. Zhang, F. Formalik, D. Lv, F. Sha, K. O. Kirlikovali, X. Wang, X. Tang, S. Su, H. Xie, Y. Chen, Z. Li, R. Q. Snurr and O. K. Farha, Lowering Linker Symmetry to Access Zirconium Metal–Organic Frameworks for Inverse Alkane/Alkene Separations, *Angew. Chem., Int. Ed.*, 2025, **14**, e20242460.

34 B. Ortín-Rubio, C. Perona-Bermejo, J. A. del Pino, F. J. Carmona, F. Gándara, J. A. R. Navarro, J. Juanhuix, I. Imaz and D. Maspoch, A mesoporous Zr-based metal-organic framework driven by the assembly of an octatopic linker, *Chem. Commun.*, 2023, **59**, 7803–7806.

35 Z. Chen, Ł. J. Weseliński, K. Adil, Y. Belmabkhout, A. Shkurenko, H. Jiang, P. M. Bhatt, V. Guillerm, E. Dauzon, D. X. Xue, M. O'Keeffe and M. Eddaoudi, Applying the Power of Reticular Chemistry to Finding the Missing alb-MOF Platform Based on the (6,12)-Coordinated Edge-Transitive Net, *J. Am. Chem. Soc.*, 2017, **139**, 3265–3274.

36 J. E. Mondloch, W. Bury, D. Fairen-Jimenez, S. Kwon, E. J. Demarco, M. H. Weston, A. A. Sarjeant, S. T. Nguyen, P. C. Stair, R. Q. Snurr, O. K. Farha and J. T. Hupp, Vapor-Phase Metalation by Atomic Layer Deposition in a Metal-Organic Framework, *J. Am. Chem. Soc.*, 2013, **135**, 10294–10297.

37 C. W. Kung, T. C. Wang, J. E. Mondloch, D. Fairen-Jimenez, D. M. Gardner, W. Bury, J. M. Klingsporn, J. C. Barnes, R. Van Duyne, J. F. Stoddart, M. R. Wasielewski, O. K. Farha and J. T. Hupp, Metal-Organic Framework Thin Films Composed of Free-Standing Acicular Nanorods Exhibiting Reversible Electrochromism, *Chem. Mater.*, 2013, **25**, 5012–5017.

38 W. Gong, Y. Geng, P. Gao, J. Zhang, K. Zhou, J. Dong, O. K. Farha and Y. Cui, Leveraging Isoreticular Principle to Elucidate the Key Role of Inherent Hydrogen-Bonding Anchoring Sites in Enhancing Water Sorption Cyclability of Zr(IV) Metal–Organic Frameworks, *J. Am. Chem. Soc.*, 2024, **146**, 21806–21814.

39 V. Quezada-Novoa, H. M. Titi, A. A. Sarjeant and A. J. Howarth, Building a shp: A Rare-Earth Metal-Organic Framework and Its Application in a Catalytic Photooxidation Reaction, *Chem. Mater.*, 2021, **33**, 4163–4169.

40 J. Yu, R. Anderson, X. Li, W. Xu, S. Goswami, S. S. Rajasree, K. Maindan, D. A. Gómez-Gualdrón and P. Deria, Improving Energy Transfer within Metal-Organic Frameworks by Aligning Linker Transition Dipoles along the Framework Axis, *J. Am. Chem. Soc.*, 2020, **142**, 11192–11202.

41 H.-L. Xia, K. Zhou, L. Yu, H. Wang, X.-Y. Liu, D. M. Proserpio and J. Li, Customized Synthesis: Solvent- and Acid-Assisted Topology Evolution in Zirconium-Tetracarboxylate Frameworks, *Inorg. Chem.*, 2022, **61**(20), 7980–7988.

42 B. Wang, Q. Yang, C. Guo, Y. Sun, L. H. Xie and J.-R. Li, Stable Zr(IV)-Based Metal-Organic Frameworks with Predesigned Functionalized Ligands for Highly Selective Detection of Fe(III) Ions in Water, *ACS Appl. Mater. Interfaces*, 2017, **9**, 10286–10295.

43 R. Luebke, Y. Belmabkhout, Ł. J. Weseliński, A. J. Cairns, M. Alkordi, G. Norton, Ł. Wojtas, K. Adil and M. Eddaoudi, Versatile Rare Earth Hexanuclear Clusters for the Design and Synthesis of Highly-Connected ftw -MOFs, *Chem. Sci.*, 2015, **6**, 4095–4102.

44 H. Wang, X. Dong, J. Lin, S. J. Teat, S. Jensen, J. Cure, E. V. Alexandrov, Q. Xia, K. Tan, Q. Wang, D. H. Olson, D. M. Proserpio, Y. J. Chabal, T. Thonhauser, J. Sun, Y. Han and J. Li, Topologically Guided Tuning of Zr-MOF Pore Structures for Highly Selective Separation of C6 Alkane Isomers, *Nat. Commun.*, 2018, **9**, 1–11.

45 D. X. Xue, A. Cadiau, Ł. J. Weseliński, H. Jiang, P. M. Bhatt, A. Shkurenko, L. Wojtas, C. Zhijie, Y. Belmabkhout, K. Adil and M. Eddaoudi, Topology Meets MOF Chemistry for Pore-Aperture Fine Tuning: ftw-MOF Platform for Energy-Efficient Separations: Via Adsorption Kinetics or Molecular Sieving, *Chem. Commun.*, 2018, **54**, 6404–6407.

46 Y. Chen, X. Zhang, M. R. Mian, F. A. Son, K. Zhang, R. Cao, Z. Chen, S. J. Lee, K. B. Idrees, T. A. Goetjen, J. Lyu, P. Li, Q. Xia, Z. Li, J. T. Hupp, T. Islamoglu, A. Napolitano, G. W. Peterson and O. K. Farha, Structural Diversity of Zirconium Metal-Organic Frameworks and Effect on Adsorption of Toxic Chemicals, *J. Am. Chem. Soc.*, 2020, **142**, 21428–21438.

47 G. K. Angeli, C. Sartsidou, S. Vlachaki, I. Spanopoulos, C. Tsangarakis, A. Kourtellaris, E. Klontzas, G. E. Froudakis, A. Tasiopoulos and P. N. Trikalitis, Reticular Chemistry and the Discovery of a New Family of Rare Earth (4,8)-Connected Metal-Organic Frameworks with csq Topology Based on $RE_4(M_3\text{-}O)_2(COO)_8$ Clusters, *ACS Appl. Mater. Interfaces*, 2017, **9**, 44560–44566.

48 M. Lammert, H. Reinsch, A. C. Murray, M. T. Wharmby, H. Terraschke and N. Stock, Synthesis and Structure of Zr(IV)- and Ce(IV)-Based CAU-24 with 1,2,4,5-Tetrakis(4-Carboxyphenyl)Benzene, *Dalton Trans.*, 2016, **45**, 18822–18826.

49 R. G. Abdulhalim, P. M. Bhatt, Y. Belmabkhout, A. Shkurenko, K. Adil, L. J. Barbour and M. Eddaoudi, A Fine-Tuned Metal-Organic Framework for Autonomous Indoor Moisture Control, *J. Am. Chem. Soc.*, 2017, **139**, 10715–10722.

50 J. Su, S. Yuan, T. Wang, C. T. Lollar, J. L. Zuo, J. Zhang and H.-C. Zhou, Zirconium Metal–Organic Frameworks Incorporating Tetrathiafulvalene Linkers: Robust and Redox-Active Matrices for in Situ Confinement of Metal Nanoparticles, *Chem. Sci.*, 2020, **11**, 1918–1925.

51 J. Su, S. Yuan, J. Li, H. Y. Wang, J. Y. Ge, H. F. Drake, C. F. Leong, F. Yu, D. M. D'Alessandro, M. Kurmoo, J. L. Zuo and H.-C. Zhou, Rare-Earth Metal Tetrathiafulvalene Carboxylate Frameworks as Redox-Switchable Single-Molecule Magnets, *Chem.–Eur. J.*, 2021, **27**, 622–627.

52 M. Abbas, S. Sheybani, M. L. Mortensen and K. J. Balkus, Fluoro-bridged rare-earth metal-organic frameworks, *Dalton Trans.*, 2024, **53**, 3445–3453.

53 A. R. B. J. Lutton-Gething, B. Spencer, G. F. S. Whitehead, I. J. Vitorica-Yrezabal, D. N. Lee and M. P. Attfield,

Disorder and Sorption Preferences in a Highly Stable Fluoride-Containing Rare-Earth fcu-Type Metal–Organic Framework, *Chem. Mater.*, 2024, **36**, 1957–1965.

54 A. R. B. J. Lutton-Gething, F. I. Pambudi, B. Spencer, D. N. Lee, G. F. S. Whitehead, I. J. Vitorica-Yrezabal and M. P. Attfield, Revealing Disorder, Sorption Locations and a Sorption-Induced Single Crystal–Single Crystal Transformation in a Rare-Earth fcu-Type Metal–Organic Framework, *Inorg. Chem.*, 2024, **63**, 22315–22322.

55 J. P. Vizuet, M. L. Mortensen, A. L. Lewis, M. A. Wunch, H. R. Firouzi, G. T. McCandless and K. J. Balkus, Fluoro-Bridged Clusters in Rare-Earth Metal-Organic Frameworks, *J. Am. Chem. Soc.*, 2021, **143**, 17995–18000.

56 M. S. Christian, K. J. Fritzsching, J. A. Harvey, D. F. S. Gallis, T. M. Nenoff and J. M. Rimsza, Dramatic Enhancement of Rare-Earth Metal-Organic Framework Stability Via Metal Cluster Fluorination, *JACS Au*, 2022, **2**, 1889–1898.

57 H. Wang, X. L. Dong, V. Colombo, Q. N. Wang, Y. Y. Liu, W. Liu, X. L. Wang, X. Y. Huang, D. M. Proserpio, A. Sironi, Y. Han and J. Li, Tailor-Made Microporous Metal-Organic Frameworks for the Full Separation of Propane from Propylene Through Selective Size Exclusion, *Adv. Mater.*, 2018, **30**, 1805088.

58 X. Li, J. Liu, K. Zhou, S. Ullah, H. Wang, J. Zou, T. Thonhauser and J. Li, Tuning Metal–Organic Framework (MOF) Topology by Regulating Ligand and Secondary Building Unit (SBU) Geometry: Structures Built on 8-Connected $M_6$ (M = Zr, Y) Clusters and a Flexible Tetracarboxylate for Propane-Selective Propane/Propylene Separation, *J. Am. Chem. Soc.*, 2022, **144**, 21702–21709.

59 H. A. Bicalho, F. Saraci, J. D. Velazquez-Garcia, H. M. Titi and A. J. Howarth, Unravelling the synthesis of a rare-earth cluster-based metal-organic framework with spn topology, *Chem. Commun.*, 2022, **58**, 10925–10928.

60 H. A. Bicalho, C. Copeman, H. P. Barbosa, P. R. Donnarumma, Z. Davis, V. Quezada-Novoa, J. D. Velazquez-Garcia, N. Liu, E. Hemmer and A. J. Howarth, Synthesis, Characterization and Photophysical Properties of a New Family of Rare-Earth Cluster-Based Metal-Organic Frameworks, *Chem.–Eur. J.*, 2024, **30**, e202402363.

61 G. K. Angeli, E. Loukopoulos, K. Kouvidis, A. Bosveli, C. Tsangarakis, E. Tylianakis, G. Froudakis and P. N. Trikalitis, Continuous Breathing Rare-Earth MOFs Based on Hexanuclear Clusters with Gas Trapping Properties, *J. Am. Chem. Soc.*, 2021, **143**, 10250–10260.

62 V. Quezada-Novoa, H. M. Titi, F. Y. Villanueva, M. W. B. Wilson and A. J. Howarth, The Effect of Linker-to-Metal Energy Transfer on the Photooxidation Performance of an Isostructural Series of Pyrene-Based Rare-Earth Metal-Organic Frameworks, *Small*, 2023, **19**, 2302173.

63 Y. Y. Zhang, X. Zhang, J. F. Lyu, K. Otake, X. J. Wang, L. R. Redfern, C. D. Malliakas, Z. Y. Li, T. Islamoglu, B. Wang and O. K. Farha, A Flexible Metal–Organic Framework with 4-Connected Zr6 Nodes, *J. Am. Chem. Soc.*, 2018, **140**, 11179–11183.

64 Z. J. Chen, L. J. Weselinski, K. Adil, Y. Belmabkhout, A. Shkurenko, H. Jiang, P. M. Bhatt, V. Guillerm, E. Dauzon, D. X. Xue, M. O'Keeffe and M. Eddaoudi, Applying the Power of Reticular Chemistry to Finding the Missing alb-MOF Platform Based on the (6,12)-Coordinated Edge -Transitive Net, *J. Am. Chem. Soc.*, 2017, **139**, 3265–3274.

65 R. G. AbdulHalim, P. M. Bhatt, Y. Belmabkhout, A. Shkurenko, K. Adil, L. J. Barbour and M. Eddaoudi, A Fine-Tuned Metal-Organic Framework for Autonomous Indoor Moisture Control, *J. Am. Chem. Soc.*, 2017, **139**, 10715–10722.

66 B. Al-Mohammadi, J. X. Wang, H. Jiang, P. Parvatkar, A. Shkurenko, P. M. Bhatt, N. Y. Tashkandi, O. Shekhah, O. F. Mohammed, M. Eddaoudi and D. Alezi, Rare Earth alb-MOFs: From Synthesis to Their Deployment for Amine-Sensing Application in Aqueous Media, *ACS Appl. Mater. Interfaces*, 2024, **17**, 17751–17756.

67 E. Loukopoulos, G. K. Angeli, C. Tsangarakis, E. Traka, K. G. Froudas and P. N. Trikalitis, Reticular Synthesis of Flexible Rare-Earth Metal-Organic Frameworks: Control of Structural Dynamics and Sorption Properties Through Ligand Functionalization, *Chem.–Eur. J.*, 2024, **30**, e202302709.

68 E. Loukopoulos, G. K. Angeli, K. Kouvidis, C. Tsangarakis and P. N. Trikalitis, Accessing 14-Connected Nets: Continuous Breathing, Hydrophobic Rare-Earth Metal Organic Frameworks Based on 14-c Hexanuclear Clusters with High Affinity for Non-Polar Vapors, *ACS Appl. Mater. Interfaces*, 2022, **14**, 22242–22251.

69 Y. Guo, L. J. Zhang, N. Muhammad, Y. Xu, Y. S. Zhou, F. Tang and S. W. Yang, Chiral Silver–Lanthanide Metal–Organic Frameworks Comprised of One-Dimensional Triple Right-Handed Helical Chains Based on [Ln7(μ3-OH)8]13+ Clusters, *Inorg. Chem.*, 2018, **57**, 995–1003.

70 W. H. Fang, L. Cheng, L. Huang and G. Y. Yang, A Series of Lanthanide-Based Cluster Organic Frameworks Made of Heptanuclear Trigonal-Prismatic Cluster Units, *Inorg. Chem.*, 2013, **52**, 6–8.

71 X. Y. Li, Y. X. Wang, J. Xie, X. M. Yin, M. A. Silver, Y. W. Cai, H. L. Zhang, L. H. Chen, G. Q. Bian, D. W. Juan, Z. F. Chai and S. Wang, Monitoring Ultraviolet Radiation Dosage Based on a Luminescent Lanthanide Metal-Organic Framework, *Inorg. Chem.*, 2018, **57**, 8714–8717.

72 P. Qu, M. H. Zhang and J. W. Zhang, A rare heptanuclear cluster-based yttrium-organic framework with an aromatic tricarboxylate ligand for blue LED application, *Inorg. Chem. Commun.*, 2023, **151**, 110623.

73 M. Li, M. O'Keeffe, D. M. Proserpio and H.-F. Zhang, A New Group of Edge-transitive 3-Periodic Nets and Their Derived Nets for Reticular Chemistry, *Cryst. Growth Des.*, 2020, **20**, 4062–4068.

74 A. Cadiau, L. S. Xie, N. Kolobov, A. Shkurenko, M. Qureshi, M. R. Tchalala, S. S. Park, A. Bavykina, M. Eddaoudi, M. Dinca, C. H. Hendon and J. Gascon, Toward New 2D Zirconium-Based Metal-Organic Frameworks: Synthesis,

Structures, and Electronic Properties, *Chem. Mater.*, 2020, **32**, 97–104.

75 *Materials Studio 2023*, Dassault Systèmes BIOVIA, San Diego, CA, 2023.

76 H. Furukawa, F. Gándara, Y. B. Zhang, J. C. Jiang, W. L. Queen, M. R. Hudson and O. M. Yaghi, Water Adsorption in Porous Metal-Organic Frameworks and Related Materials, *J. Am. Chem. Soc.*, 2014, **136**, 4369–4381.

77 M. W. Zhang, Y. P. Chen, M. Bosch, T. Gentle, K. C. Wang, D. W. Feng, Z. Y. U. Wang and H. C. Zhou, Symmetry-Guided Synthesis of Highly Porous Metal-Organic Frameworks with Fluorite Topology, *Angew. Chem., Int. Ed.*, 2014, **53**, 815–818.

78 M. Schulz, A. Gehl, J. Schlenkrich, H. A. Schulze, S. Zimmermann and A. Schaate, A Calixarene-Based Metal–Organic Framework for Highly Selective $NO_2$ Detection, *Angew. Chem., Int. Ed.*, 2018, **57**, 12961–12965.

79 R. S. H. Khoo, C. Fiankor, S. Z. Yang, W. H. Hu, C. Q. Yang, J. Z. Lu, M. D. Morton, X. Zhang, Y. Liu, J. R. Huang and J. Zhang, Postsynthetic Modification of the Nonanuclear Node in a Zirconium Metal-Organic Framework for Photocatalytic Oxidation of Hydrocarbons, *J. Am. Chem. Soc.*, 2023, **145**, 24052–24060.

80 G. K. Angeli, D. Batzavali, K. Mavronasou, C. Tsangarakis, T. Stuerzer, H. Ott and P. N. Trikalitis, Remarkable Structural Diversity between Zr/Hf and Rare-Earth MOFs via Ligand Functionalization and the Discovery of Unique (4,8)-c and (4,12)-connected Frameworks, *J. Am. Chem. Soc.*, 2020, **142**, 15986–15994.

81 X. Zhang, X. Zhang, J. A. Johnson, Y. S. Chen and J. Zhang, Highly Porous Zirconium Metal–Organic Frameworks with β-UH3-like Topology Based on Elongated Tetrahedral Linkers, *J. Am. Chem. Soc.*, 2016, **138**, 8380–8383.

82 Y. Yan, A. E. O'Connor, G. Kanthasamy, G. Atkinson, D. R. Allan, A. J. Blake and M. Schröder, Unusual and Tunable Negative Linear Compressibility in the Metal-Organic Framework MFM-133(M) (M = Zr, Hf), *J. Am. Chem. Soc.*, 2018, **140**, 3952–3958.

83 E. López-Maya, C. Montoro, L. M. Rodríguez-Albelo, S. D. Aznar Cervantes, A. A. Lozano-Pérez, J. L. Cenís, E. Barea and J. A. R. Navarro, Textile/Metal–Organic-Framework Composites as Self-Detoxifying Filters for Chemical-Warfare Agents, *Angew. Chem., Int. Ed.*, 2015, **54**, 6790–6794.

84 T. Islamoglu, Z. Chen, M. C. Wasson, C. T. Buru, K. O. Kirlikovali, U. Afrin, M. R. Mian and O. K. Farha, Metal–Organic Frameworks against Toxic Chemicals, *Chem. Rev.*, 2020, **120**, 8130–8160.

85 R. Gil-San-Millan, E. López-Maya, A. E. Platero-Prats, V. Torres-Pérez, P. Delgado, A. W. Augustyniak, M. K. Kim, H. W. Lee, S. G. Ryu and J. A. R. Navarro, Magnesium Exchanged Zirconium Metal–Organic Frameworks with Improved Detoxification Properties of Nerve Agents, *J. Am. Chem. Soc.*, 2019, **141**, 11801–11805.

86 E. Borrego-Marin, P. Garrido-Barros, G. W. Peterson, R. Vismara, F. J. Carmona, E. Barea and J. A. R. Navarro, Reactive ZIF-L Crystal Surface for Organophosphorous Degradation and Acetylcholinesterase Reactivation, *J. Am. Chem. Soc.*, 2025, **147**(13), 10834–10839.

87 J.-H. Lee, W.-J. Kim, D. Park, Y. Jo, J. H. Baik and Y.-W. Suh, Zirconia-incorporated yttria with a Lewis pair of acid–base surface sites for chemoselective dehydration of alcohols into alpha olefins, *Appl. Catal., A*, 2024, **678**, 119707.

88 (*a*) CCDC 2470518: Experimental Crystal Structure Determination, 2025, DOI: **10.5517/ccdc.csd.cc2nxs4j**; (*b*) CCDC 2470519: Experimental Crystal Structure Determination, 2025, DOI: **10.5517/ccdc.csd.cc2nxs5k**; (*c*) CCDC 2470520: Experimental Crystal Structure Determination, 2025, DOI: **10.5517/ccdc.csd.cc2nxs6l**; (*d*) CCDC 2470521: Experimental Crystal Structure Determination, 2025, DOI: **10.5517/ccdc.csd.cc2nxs7m**; (*e*) CCDC 2470522: Experimental Crystal Structure Determination, 2025, DOI: **10.5517/ccdc.csd.cc2nxs8n**; (*f*) CCDC 2472930: Experimental Crystal Structure Determination, 2025, DOI: **10.5517/ccdc.csd.cc2p08yy**.